Supplementary Materials

Effects on global warming by microbial methanogenesis in alkaline lakes during the Late Paleozoic Ice Age (LPIA)

Liuwen Xia[1], Jian Cao[1*], Wenxuan Hu[1], Eva E. Stüeken[2], Xiaolin Wang[1], Suping Yao[1], Dongming Zhi[3], Yong Tang[3], Baoli Xiang[3], Wenjun He[3]

1 *School of Earth Sciences and Engineering, Nanjing University, Nanjing, Jiangsu 210023, China*

2. *School of Earth & Environmental Sciences, University of St Andrews, St Andrews, Fife, KY16 9AL Scotland, UK*

3 *PetroChina Xinjiang Oilfield Company, Karamay, Xinjiang 843000, China*

This file includes:

[1] Geological setting and samples

[1.1] *Geological setting*

Zircon U–Pb dating shows that the Fengcheng Formation in the Mahu Sag was deposited from 305–296 Ma (Wang et al., 2020, 2022b), overlapping with a rapid warming event at *ca*. 304 Ma (Richey et al., 2020; Chen et al., 2022; Montañez, 2022), and thus the formation is an important archive for investigating global warming mechanisms (Cao et al., 2020; Wu et al., 2021; Wang et al., 2022a). The organic-rich, alkaline lacustrine sedimentary rocks of the Lucaogou Formation (292–288 Ma) in the Jimusar Sag, southeastern Junggar Basin (Wu et al., 2021; Xia et al., 2021a; Wang et al., 2022a), were deposited during the end of the LPIA (after *ca.* 290 Ma) and can be compared with the Fengcheng Formation.

The Fengcheng Formation was deposited in a post-orogenic fault depression developed on Paleozoic basement in the northwestern Junggar Basin, and it comprises a series of fan–delta–lacustrine sediments (Fig. 1) (Carroll, 1998; Yu et al., 2018; Cao et al., 2020). The Fengcheng Formation was deposited in an evaporitic, alkaline lacustrine environment characterized by anoxic, hypersaline, and stratified water

conditions, abundant volcanic ash, and deep hydrothermal activity in a (semi-)arid climate (Cao et al., 2020; Wang et al., 2021). Evidence for the alkaline lacustrine setting include diagnostic alkali minerals, including trona ($Na_2CO_3.NaHCO_3.2H_2O$), nahcolite ($NaHCO_3$), wegscheiderite ($Na_5H_3[CO_3]_4$), and shortite ($Na_2Ca_2[CO_3]_3$), abundant spheroidal bacteria-like fossils, low clay mineral contents, and complete sedimentary evolutionary sequence of an alkaline lake (i.e., the early onset, preliminary, strong, and weak–terminal stages of alkalinity) (Cao et al., 2020). Previous studies found that the average $\delta^{15}N$ value of the Fengcheng Formation is 18.4‰, with values as high as 22.6‰ (Xia et al., 2020), which are within the range of $\delta^{15}N$ values for modern alkaline lakes (>10‰; the average and highest values are 13.7‰ and 28.0‰, respectively) (Stüeken et al., 2015, 2020). The high $\delta^{15}N$ values of the Fengcheng Formation are due to strong ammonia volatilization that can only occur when the pH exceeds 9.25 (Li et al., 2012, 2021; Deng et al., 2018), which shows that the Fengcheng Formation was deposited in an ancient, alkaline lacustrine setting with a high pH. Mineralogical study showed that the anions in the lake water were mainly HCO_3^- and CO_3^{2-}, while [SO_4^{2-}] was lower than 12.5–13.5 mM (calculated from the gypsum solubility of 2.4–2.6 g/L under temperature of 10–30 ◦C) during deposition of the Fengcheng Formation in the Junggar Basin (Yu et al., 2018; Cao et al., 2020; Wang et al., 2020). This is because the evaporitic minerals in the Fengcheng Formation are alkali minerals, whereas sulfate minerals such as gypsum ($CaSO_4.2H_2O$) and anhydrite ($CaSO_4$) are rare or absent (Wang et al., 2020).

The Fengcheng Formation is characterized by significant spatial heterogeneity and can be divided into three major areas (Fig. 1). The lake center, where a large amount of alkali minerals developed, is called the central salt rock area (CSR) and was sampled by wells F20, FN3, FN5, FN7, and AK1. The transition area comprises mainly dolomitic rocks and is called the transitional dolomite area (TD, wells F5, FN1, and FN14). The marginal area consists mainly of tuffaceous mudstone and is called the marginal tuff–mudstone area (MTM, wells X40, X76, and X87) (Xia et al., 2020; Wang et al., 2021). The Fengcheng Formation is further divided into First (F_1), Second (F_2), and Third (F_3) members (from bottom to top) (Cao et al., 2020; Xia et al., 2020). In the CSR (from bottom to top), the lower part of F_1 is dominated by mudstone, and the upper part of F_1 is composed of carbonates in which calcite and then dolomite is predominant. In the upper part of F_1, the content of dolomitic rocks is high, which reflects the gradual increase in salinity of the lake water. Moreover, small amounts of transitional Na carbonate minerals, such as shortite, were deposited locally in the upper part of F_1, indicating that it had become an alkaline lake. F_2 is characterized by abundant evaporitic Na-carbonate minerals, reflecting the peak of alkalinity. In F_3, the content of dolomitic rocks and alkali minerals decrease gradually, which reflects the weak–terminal stages of alkalinity (Cao et al., 2020; Xia et al., 2020).

The Lucaogou Formation is mainly located in the Jimusar Sag and other areas in the southeastern Junggar Basin and was deposited in a dustpan-shaped sag developed on folded basement in the Middle Carboniferous. The Lucaogou Formation was mainly deposited in a nearshore-shallow to fairly deep lacustrine setting where abundant volcanic ash was present and hydrothermal activity was occurring (Liu et al., 2019; Jiang et al., 2020; Wu et al., 2021; Wang et al., 2022a). Compared with the Fengcheng Formation, the Lucaogou Formation had a lower salinity and was more oxygenated, but it was also alkaline. Evidence that the Lucaogou Formation was deposited in an early-stage alkaline lake includes sporadic development of transitional Na carbonate minerals (e.g., shortite) and high $\delta^{15}N$ values (10.6‰–16.8‰) (Xia et al., 2021a). The Lucaogou Formation consists of fine-grained, multi-source, mixed sediments including sandstones, mudstones, carbonates, and tuff, which are organic-rich (Su et al., 2019; Wang et al., 2021).

[1.2] *Sample description*

Thirty core samples were collected from 5 wells (F20, FN3, FN5, FN7, and AK1) in the CSR; 14 samples were collected from 3 wells (F5, FN1, and FN14) in the TD; and 8 samples were collected from 3 wells (X40, X76, and X87) in the MTM (Fig. 1; Table S2). The CSR area was used to study the temporal variations in the Fengcheng Formation. The samples from well F20 and one sample from well FN3 are from F_3 (i.e., a total of 13 samples). The samples from wells FN5 and FN7, and one sample from well FN3 are from F_2 (i.e., a total of 11 samples). The samples from well AK1 are from F_1 (i.e., a total of 6 samples). See the detailed sample descriptions from (Xia et al., 2020, 2021b).

[2] Methods

[2.1] *Sulfur isotopes*

Bulk and pyrite S isotope data were obtained at the School of Earth and Environmental Sciences, University of St Andrews, Scotland, UK. For the whole-rock analyses, 2 M HCl was first added to the dried sample powders (< 200 mesh) at 25°C and left overnight to remove carbonates. The resulting residues were washed three times in >18 MΩ cm^{-1} H_2O, and then dried in an oven overnight at 60°C. Pyrite-bound S was extracted using the Cr reduction method on a separate aliquot of powder (Canfield et al., 1986). The samples were boiled with a mixture of concentrated 6 M HCl (15 mL) and 1 M $CrCl_2$ (in 0.5 M HCl; 35 mL) under a constant stream of N_2 gas for 2 h. The H_2S generated during the reaction between the pyrite and Cr^{2+} was trapped with a solution of 3% $AgNO_3$ in 10% NH_4OH. The Ag_2S precipitate was dried at 45°C in a closed oven.

Decarbonated bulk and Ag_2S powders were then weighed into Sn capsules and analyzed by flash combustion in an elemental analyzer (EA Isolink) coupled to an isotope ratio mass spectrometer (Thermo Finnigan MAT253) via a Conflo IV. IAEA-S1, IAEA-S2, and IAEA-S3 were used as the in-house standards. The reproducibility was ±1.2‰ (1 SD). Results are expressed in delta notation relative to VCDT: $\delta^{34}S$ [in ‰] = $(^{34/32}S_{sample}/^{34/32}S_{standard} - 1) \times 1000$.

[2.2] *Extraction and fractionation of biomarkers*

Biomarker analyses were conducted at Nanjing University, Nanjing, China, on large pieces of intact drill core from which the external surfaces were carefully removed by sawing to isolate inner core portions. The crushed rock powders were first extracted in a CEM microwave accelerated reaction system (MARS 6) at 100°C in a 9:1 (v/v) dichloromethane (DCM) and methanol (MeOH) mixture for 15 min with constant stirring. This yielded the rock bitumen. Elemental S was removed from the rock bitumen using HCl-activated and solvent-rinsed Cu pellets. The desulfurized rock bitumen was further separated using dry-packed silica gel (36–70 mesh and activated at 450°C overnight) column chromatography into aliphatic, aromatic, and polar fractions. The aliphatic hydrocarbon fraction was eluted with *n*-hexane, followed by the aromatic fraction with 1:1 (v/v) *n*-hexane and DCM, and the polar fraction with 3:1 (v/v) DCM and MeOH (v/v) on dry-packed silica gel microcolumns.

[2.3] *Gas chromatography-isotope ratio mass spectrometry*

Aliphatic hydrocarbon fractions were analyzed at Nanjing University, Nanjing, China, using gas chromatography-isotope ratio mass spectrometry (GC-IRMS). GC-IRMS analysis was carried out using a Thermo Scientific Trace GC 1310 interfaced to a Thermo Scientific Delta Plus V isotope ratio mass spectrometer. The GC was fitted with a 30 m × 0.32 mm i.d. HP-5 column with a film thickness of 0.25 μm using He as the carrier gas. The initial temperature was 60 ◦C held for 5 min, and then programmed to 295

◦C at 3 ◦C/min, followed by a 30 min isothermal hold. The injection of samples was conducted in the splitless mode at 310 ◦C. The instrument stability was monitored by regular analysis of an in-house gas (CO_2) standard. Samples were measured in duplicate with a reproducibility of typically <1–2‰. The isotopic ratios are reported relative to the Vienna Peedee belemnite (V-PDB) standard: $\delta^{13}C$ [‰]= ($^{13/12}C_{sample}/^{13/12}C_{standard} - 1$) ×1000.

[3] Results

[3.1] *Compiled data from previous studies*

To investigate the CH_4 cycling in ancient alkaline lakes in the Junggar Basin, this study also examined published total ion chromatograms, MRM-GC-MS chromatograms, and 3β-MeHI values of organic-rich Fengcheng Formation sedimentary rocks (Table S1; Fig. S2) (Xia et al., 2021b), along with organic C isotopes ($\delta^{13}C_{org}$), carbonate C isotopes ($\delta^{13}C_{carb}$), and total S/total organic C (TS/TOC) ratios (Table S1) (Xia et al., 2020).

The 3β-MeHI values of the Fengcheng Formation are: CSR mean = 7.0% ± 3.3% > TD mean = 5.4% ± 3.0% > MTM mean = 4.1% ± 2.7%). In the CSR, the 3β-MeHI values of F_3 (mean = 9.5% ± 3.0%) are significantly higher than those of F_1 (mean = 7.7% ± 3.6%) and F_2 (mean = 4.9% ± 2.3%). $\delta^{13}C_{org}$ values do not vary significantly either spatially or vertically, but $\delta^{13}C_{carb}$ values in the CSR (mean = 3.3‰ ± 1.3‰) and TD (mean = 4.2‰ ± 1.4‰) are significantly higher than those of the MTM (mean = –1.4‰ ± 1.9‰). $\delta^{13}C_{carb}$ values of F_3 (mean = 4.5‰ ± 0.8‰) in the CSR are significantly higher than those of F_1 (mean = 2.3‰ ± 0.5‰) and F_2 (mean = 2.3‰ ± 0.6‰). TS/TOC ratios do not exhibit significant spatial variability. In the CSR, TS/TOC ratios decrease gradually up-section with F_1 (mean = 1.6 ± 0.6) > F_2 (mean = 1.0 ± 0.5) > F_3 (mean = 0.2 ± 0.1).

[3.2] *Sulfur isotope data*

The whole-rock S isotope data ($\delta^{34}S_{bulk}$) of the organic-rich deposits in the Fengcheng Formation do not exhibit significant spatial variability (Table S1; Fig. S3A). In the CSR, $\delta^{34}S_{bulk}$ values increase gradually up-section: F_1 (mean = –19.3‰ ± 4.6‰) < F_2 (mean = –9.1‰ ± 1.7‰) < F_3 (mean = 2.8‰ ± 10.5‰). $\delta^{34}S_{bulk}$ values exhibit a strong negative correlation with TS/TOC ratios (Fig. S3A; r = –0.71). Fifteen samples with high total S contents were selected for pyrite S isotope analysis ($\delta^{34}S_{py}$), and it was found that the $\delta^{34}S_{bulk}$ and $\delta^{34}S_{py}$ values of a single sample were approximately the same (r = +0.99). Therefore, the whole-rock S contents of the samples is mainly S in pyrite, and $\delta^{34}S_{bulk}$ approximately represents the $\delta^{34}S_{py}$ values (Fig. S3B). This good match also provides additional confidence in the accuracy of our data, despite the relatively large analytical standard deviation for bulk rock analyses.

[3.3] *$\delta^{13}C$ data for the hydrocarbons*

$\delta^{13}C$ values of *n*-alkanes, isoprenoids, steranes, and hopanes from the Fengcheng Formation samples are shown in Fig. S1, and there are few differences between the CSR, TD, and MTM. $C_{16–21}$ *n*-alkanes, pristane (Pr), phytane (Ph), and β-carotane are mainly derived from aquatic primary producers such as green algae and cyanobacteria (Borowitzka et al., 1990; Hayes et al., 1990; Peters et al., 2005), and C_{21} regular isoprenoids (*i*-C_{21}) may reflect the population of halophilic archaea feeding on aquatic primary producers (McKirdy et al., 1984; Grice et al., 1998). All these compounds have $\delta^{13}C$ values of –29‰ to –33‰ with no significant spatial and temporal variations (Fig. S1). For the $C_{22–29}$ *n*-alkanes from terrestrial higher plants or mixed sources with aquatic primary producers (Peters et al., 2005; Correction Pagani et al., 2006), the $\delta^{13}C$ values in the TD and MTM are slightly lower than those in the CSR. Previous studies have

shown that the regular steranes in the Fengcheng Formation are mainly C_{28} and C_{29}, which may be derived from haloalkaliphilic green algae (Xia et al., 2021b). $\delta^{13}C$ values of regular steranes vary from –33‰ to –45‰, with no clear spatial variation, and a slight increase up-section (Fig. S1). $\delta^{13}C$ values of regular hopanes from the Fengcheng Formation are highly negative. For example, $\delta^{13}C$ values of the C_{31} regular hopanes are –44‰ to –61‰ (Fig. S1), which are similar to the $\delta^{13}C$ values of regular hopanes in the organic-rich deposits in the Lucaogou Formation in the southeastern Junggar Basin (–44.4‰ to –55.6‰) (Sun et al., 2022).

[4] Mechanisms for proxies to constrain the [SO_4^{2-}] and [DIC]

In this study, TS/TOC ratios and $\delta^{34}S$ values were used to further constrain the [SO_4^{2-}] in the alkaline lakes and its possible effects on microbial CH_4 production. The specific mechanisms are as follows. Firstly, dissimilatory microbial sulfate reduction (MSR) produces H_2S in anoxic bottom waters and sediments by oxidizing organic matter, which then reacts with highly reactive Fe to produce pyrite (Fike et al., 2015). Given that most sulfate is deposited in reduced forms such as pyrite S and organic S (as sulfate minerals are absent), the [SO_4^{2-}] in the sedimentary waters can be assumed to correlate with TS/TOC ratios (Berner and Raiswell, 1984; Wei and Algeo, 2019). Secondly, sulfur isotopes can be used to constrain the relative size of the sulfate reservoir, as $\delta^{34}S$ values tend to increase as a consequence of Rayleigh distillation in settings where sulfate becomes limiting (Fike et al., 2015). We can thus use these two tools to determine relative trends in sulfate abundances in our studied sections.

$\Delta\delta^{13}C$ values ($\delta^{13}C_{carb} - \delta^{13}C_{Pr\text{-}Ph}$), where $\delta^{13}C_{carb}$ and $\delta^{13}C_{Pr\text{-}Ph}$ are carbon isotopes of carbonates and average of pristane and phytane, were used to assess the [DIC] in the alkaline lake waters and its possible effects on microbial CH_4 production In this study (Hollander and McKenzie, 1991; Freeman and Hayes, 1992; Naafs et al., 2016). The method relies on the observation that higher [DIC] in lake water causes greater discrimination against ^{13}C during algal photosynthesis, leading to more depleted $\delta^{13}C$ values in aquatic primary producers (e.g., $\delta^{13}C_{Pristane}$ ($\delta^{13}C_{Pr}$) and $^{3}C_{Phytane}$ ($\delta^{13}C_{Ph}$) where pristane and phytane is derived from chlorophylls *a* and *b*) as compared with carbonates ($\delta^{13}C_{carb}$) (Naafs et al., 2016; Witkowski et al., 2018).

[5] Evaluation of microbial CH_4 emissions

We performed a simple calculation of how much microbial CH_4 was emitted to the atmosphere from the entire lake basin. The widely studied Lake Matano, Indonesia, is a stratified anoxic modern lake with iron-rich and sulfate-free waters, and can be used as an analogue for the LPIA lakes in the Junggar Basin (Kuntz et al., 2015). Based on a box model of the carbon cycle in Lake Matano, 9–10% of organic carbon degraded via methanogenesis (Kuntz et al., 2015), so the microbial CH_4 emissions can be calculated by $E_{CH4}=M_{OC}* f_{MG}*1/2*(1-f_{MO})$, E_{CH4}=total mass of microbial CH_4 emitted; M_{OC}=total mass of organic carbon buried; f_{MG}= fraction of organic carbon degraded via methanogenesis (9–10%); f_{MO}=fraction of methane undergoing oxidation by methanotrophs. The term 1/2 accounts for the fact that the methanogenesis pathway produces CO_2 and CH_4 in equal amounts. The published field measurements of f_{MO} ranged from 54% to 94% in lakes (Kankaala et al., 2007; Schubert et al., 2012). The total mass of organic carbon buried can be calculated by M_{OC}=lake area * stratigraphic thickness * sediment density * TOC. The Fengcheng Formation in the Junggar Basin covers an area of ~5200 km^2, with an average thickness of ~260 m (well data). Based on an average density for argillaceous carbonates of 2.5 × 10^3 kg/m^3 and an average TOC content of ~2.0 wt.%, the amount of M_{OC} is estimated to be ~68 Gt. The microbial CH_4 emissions from Fengcheng Formation can be as high as ~0.2–2.1 Gt and this could be

considerable CH_4 emissions, considering emissions from many other similar terrestrial environments during the LPIA and the underestimation of buried organic carbon as original sedimentary TOC values may have been even higher than the TOC remaining of ~2.0 wt.%.

[6] References

Berner, R.A., and Raiswell, R., 1984, Geology C / S method for distinguishing freshwater from marine sedimentary rocks Geological Society of America C / S method for distinguishing freshwater from marine sedimentary rocks: Geology, v. 12, p. 365–368, doi:10.1130/0091-7613(1984)12<365.

Borowitzka, M.A., Borowitzka, L.J., and Kessly, D., 1990, Effects of salinity increase on carotenoid accumulation in the green alga Dunaliella salina: Journal of Applied Phycology, v. 2, p. 111–119, doi:10.1007/BF00023372.

Canfield, D.E., Raiswell, R., Westrich, J.T., Reaves, C.M., and Berner, R.A., 1986, The use of chromium reduction in the analysis of reduced inorganic sulfur in sediments and shales: Chemical Geology, v. 54, p. 149–155, doi:10.1016/0009-2541(86)90078-1.

Cao, J., Xia, L., Wang, T., Zhi, D., Tang, Y., and Li, W., 2020, An alkaline lake in the Late Paleozoic Ice Age (LPIA): A review and new insights into paleoenvironment and petroleum geology: Earth-Science Reviews, v. 202, p. 1–14, doi:10.1016/j.earscirev.2020.103091.

Carroll, A.R., 1998, Upper Permian lacustrine organic facies evolution, Southern Junggar Basin, NW China: Organic Geochemistry, v. 28, p. 649–667, doi:10.1016/S0146-6380(98)00040-0.

Chen, J. et al., 2022, Marine anoxia linked to abrupt global warming during Earth's penultimate icehouse: Proceedings of the National Academy of Sciences of the United States of America, v. 119, p. e2115231119, doi:10.1073/pnas.2115231119.

Correction Pagani, M. et al., 2006, Arctic hydrology during global warming at the Palaeocene/Eocene thermal maximum: Nature, v. 442, p. 671–675, doi:10.1038/nature05043.

Deng, Y., Li, Y., and Li, L., 2018, Experimental investigation of nitrogen isotopic effects associated with ammonia degassing at 0–70 °C: Geochimica et Cosmochimica Acta, v. 226, p. 182–191, doi:10.1016/j.gca.2018.02.007.

Fike, D.A., Bradley, A.S., and Rose, C. V., 2015, Rethinking the ancient sulfur cycle: Annual Review of Earth and Planetary Sciences, v. 43, p. 593–622, doi:10.1146/annurev-earth-060313-054802.

Freeman, K.H., and Hayes, J.M., 1992, Fractionation of carbon isotopes by phytoplankton and estimates of ancient CO2 levels: Global Biogeochemical Cycles, v. 6, p. 185–198, doi:10.1029/92GB00190.

Grice, K., Schouten, S., Nissenbaum, A., Charrach, J., and Sinninghe Damsté, J.S., 1998, Isotopically heavy carbon in the C21 to C25 regular isoprenoids in halite-rich deposits from the Sdom Formation, Dead Sea Basin, Israel: Organic Geochemistry, v. 28, p. 349–359, doi:10.1016/S0146-6380(98)00006-0.

Hayes, J.M., Freeman, K.H., Popp, B.N., and Hoham, C.H., 1990, Compound-specific isotopic analyses: A novel tool for reconstruction of ancient biogeochemical processes: Organic Geochemistry, v. 16, p. 1115–1128, doi:10.1016/0146-6380(90)90147-R.

Hollander, D.J., and McKenzie, J.A., 1991, CO 2 control on carbon-isotope fractionation during aqueous photosynthesis: a paleo-pCO 2 barometer: Geology, v. 19, p. 929–932, doi:10.1130/0091-7613(1991)019<0929:CCOCIF>2.3.CO;2.

Jiang, Y., Hou, D., Li, H., Zhang, Z., and Guo, R., 2020, Impact of the Paleoclimate, Paleoenvironment, and Algae Bloom: Organic Matter Accumulation in the Lacustrine Lucaogou Formation of Jimsar Sag, Junggar Basin, NW China: Energies, v. 13, p. 1488, doi:10.3390/en13061488.

Kankaala, P., Taipale, S., Nykänen, H., and Jones, R.I., 2007, Oxidation, efflux, and isotopic fractionation of

methane during autumnal turnover in a polyhumic, boreal lake: Journal of Geophysical Research: Biogeosciences, v. 112, doi:10.1029/2006JG000336.

Kuntz, L.B., Laakso, T.A., Schrag, D.P., and Crowe, S.A., 2015, Modeling the carbon cycle in Lake Matano: Geobiology, v. 13, p. 454–461, doi:10.1111/gbi.12141.

Li, L., He, Y., Zhang, Z., and Liu, Y., 2021, Nitrogen isotope fractionations among gaseous and aqueous NH4+, NH3, N2, and metal-ammine complexes: Theoretical calculations and applications: Geochimica et Cosmochimica Acta, v. 295, p. 80–97, doi:10.1016/j.gca.2020.12.010.

Li, L., Lollar, B.S., Li, H., Wortmann, U.G., and Lacrampe-Couloume, G., 2012, Ammonium stability and nitrogen isotope fractionations for NH4+-NH 3(aq)-NH 3(gas) systems at 20-70°C and pH of 2-13: Applications to habitability and nitrogen cycling in low-temperature hydrothermal systems: Geochimica et Cosmochimica Acta, v. 84, p. 280–296, doi:10.1016/j.gca.2012.01.040.

Liu, C., Liu, K., Wang, X., Wu, L., and Fan, Y., 2019, Chemostratigraphy and sedimentary facies analysis of the Permian Lucaogou Formation in the Jimusaer Sag, Junggar Basin, NW China: Implications for tight oil exploration: Journal of Asian Earth Sciences, v. 178, p. 96–111, doi:10.1016/j.jseaes.2018.04.013.

McKirdy, D.M., Kantsler, A.J., Emmett, J.K., and Aldridge, A.K., 1984, Hydrocarbon genesis and organic facies in Cambrian carbonates of the eastern Officer Basin, South Australia: Petroleum Geochemistry and Source Rock Potential of Carbonate Rocks., p. 13–32.

Montañez, I.P., 2022, Current synthesis of the penultimate icehouse and its imprint on the Upper Devonian through Permian stratigraphic record: Geological Society Special Publication, v. 512, p. 213–245, doi:10.1144/SP512-2021-124.

Naafs, B.D.A., Castro, J.M., De Gea, G.A., Quijano, M.L., Schmidt, D.N., and Pancost, R.D., 2016, Gradual and sustained carbon dioxide release during Aptian Oceanic Anoxic Event 1a: Nature Geoscience, v. 9, p. 135–139, doi:10.1038/ngeo2627.

Peters, K.E., Walters, C.C., and Moldowan, J.M., 2005, 2nd Edition of The Biomarker Guide: 700 p., doi:10.1017/cbo9780511524868.

Richey, J.D., Montañez, I.P., Goddéris, Y., Looy, C. V., Griffis, N.P., and Dimichele, W.A., 2020, Influence of temporally varying weatherability on CO2-climate coupling and ecosystem change in the late Paleozoic: Climate of the Past, v. 16, p. 1759–1775, doi:10.5194/cp-16-1759-2020.

Schubert, C.J., Diem, T., and Eugster, W., 2012, Methane emissions from a small wind shielded lake determined by eddy covariance, flux chambers, anchored funnels, and boundary model calculations: A comparison: Environmental Science and Technology, v. 46, p. 4515–4522, doi:10.1021/es203465x.

Stüeken, E.E., Buick, R., and Schauer, A.J., 2015, Nitrogen isotope evidence for alkaline lakes on late Archean continents: Earth and Planetary Science Letters, v. 411, p. 1–10, doi:10.1016/j.epsl.2014.11.037.

Stüeken, E.E., Tino, C., Arp, G., Jung, D., and Lyons, T.W., 2020, Nitrogen isotope ratios trace high-pH conditions in a terrestrial Mars analog site: Science advances, v. 6, p. eaay3440, doi:10.1126/sciadv.aay3440.

Su, Y., Zha, M., Ding, X., Qu, J., Gao, C., Jin, J., and Iglauer, S., 2019, Petrographic, palynologic and geochemical characteristics of source rocks of the Permian Lucaogou formation in Jimsar Sag, Junggar Basin, NW China: Origin of organic matter input and depositional environments: Journal of Petroleum Science and Engineering, v. 183, p. 106364, doi:10.1016/j.petrol.2019.106364.

Sun, F., Hu, W., Zhang, Z., and Cao, J., 2022, Isotopic evidence for the formation of 25-norhopanes via in situ biodegradation in the Permian Lucaogou shales, southern Junggar Basin: Organic Geochemistry, v. 163, p. 104334, doi:10.1016/j.orggeochem.2021.104334.

Wang, T., Cao, J., Carroll, A.R., Zhi, D., Tang, Y., Wang, X., and Li, Y., 2020, Oldest preserved sodium

carbonate evaporite: Late Paleozoic Fengcheng Formation, Junggar Basin, NW China: GSA Bulletin, v. 133, p. 1465–1482, doi:10.1130/b35727.1.

Wang, T., Cao, J., Jin, J., Xia, L., Xiang, B., Ma, W., and Li, W., 2021, Spatiotemporal evolution of a Late Paleozoic alkaline lake in the Junggar: Marine and Petroleum Geology, v. 124, p. 104799, doi:10.1016/j.marpetgeo.2020.104799.

Wang, Y., Cao, J., Tao, K., Xiao, W., Xiang, B., and Li, E., 2022a, Absence of β -carotane as proxies of hydrothermal activity in brackish lacustrine sediments: Palaeogeography, Palaeoclimatology, Palaeoecology, v. 587, p. 110801, doi:10.1016/j.palaeo.2021.110801.

Wang, T., Cao, J., Xia, L., Zhi, D., Tang, Y., and He, W., 2022b, Revised age of the Fengcheng Formation, Junggar Basin, China: Global implications for the late Paleozoic ice age: Global and Planetary Change, v. 208, p. 103725, doi:10.1016/j.gloplacha.2021.103725.

Wei, W., and Algeo, T.J., 2019, Elemental proxies for paleosalinity analysis of ancient shales and mudrocks: Geochimica et Cosmochimica Acta, v. 287, p. 341–366, doi:10.1016/j.gca.2019.06.034.

Witkowski, C.R., Weijers, J.W.H., Blais, B., Schouten, S., and Sinninghe Damsté, J.S., 2018, Molecular fossils from phytoplankton reveal secular PCO2 trend over the phanerozoic: Science Advances, v. 4, p. 1–8, doi:10.1126/sciadv.aat4556.

Wu, H., Hu, W., Wang, Y., Tao, K., Tang, Y., Cao, J., Wang, X., and Kang, X., 2021, Depositional conditions and accumulation models of tight oils in the middle Permian Lucaogou Formation in Junggar Basin, northwestern China: New insights from geochemical analysis: AAPG Bulletin, v. 105, p. 2477–2518, doi:10.1306/06222118094.

Xia, L., Cao, J., Hu, W., Zhi, D., Tang, Y., Li, E., and He, W., 2021a, Coupling of paleoenvironment and biogeochemistry of deep-time alkaline lakes: A lipid biomarker perspective: Earth-Science Reviews, v. 213, p. 103499, doi:10.1016/j.earscirev.2020.103499.

Xia, L., Cao, J., Lee, C., Stüeken, E.E., Zhi, D., and Love, G.D., 2021b, A new constraint on the antiquity of ancient haloalkaliphilic green algae that flourished in a ca. 300 Ma Paleozoic lake: Geobiology, v. 19, p. 147–161, doi:10.1111/gbi.12423.

Xia, L., Cao, J., Stüeken, E.E., Zhi, D., Wang, T., and Li, W., 2020, Unsynchronized evolution of salinity and pH of a Permian alkaline lake influenced by hydrothermal fluids : A multi-proxy geochemical study: Chemical Geology, v. 541, p. 119581, doi:10.1016/j.chemgeo.2020.119581.

Yu, K., Cao, Y., Qiu, L., Sun, P., Jia, X., and Wan, M., 2018, Geochemical characteristics and origin of sodium carbonates in a closed alkaline basin: The Lower Permian Fengcheng Formation in the Mahu Sag, northwestern Junggar Basin, China: Palaeogeography, Palaeoclimatology, Palaeoecology, v. 511, p. 506–531, doi:10.1016/j.palaeo.2018.09.015.

[7] Supplementary figures and tables

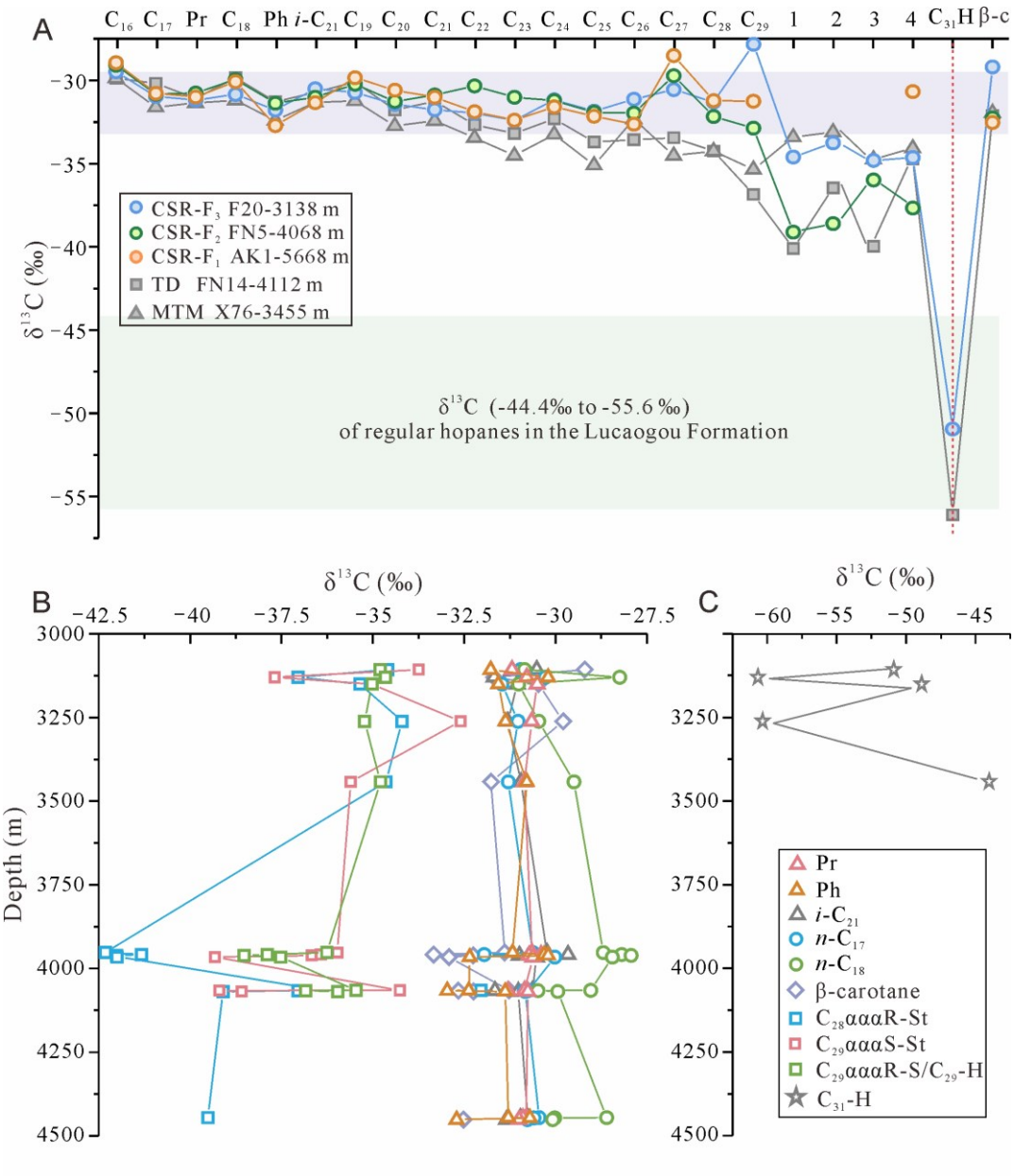

Fig. S1. Compound-specific C isotopic compositions of organic matter in the Fengcheng Formation. (A) Spatial variations; (B) stratigraphic variations of *n*-alkanes, isoprenoids, β-carotane, and regular steranes in the CSR area; (C) stratigraphic variations of C_{31} hopanes in the CSR area. 1 = C_{28}ααα20 sterane R; 2 = C_{29} ααα20S sterane; 3 = C_{29}ααα20S sterane + C_{29}αβ hopane; 4 = C_{31} *n*-alkane + C_{30}αβ hopane; $C_{16–29}$ = $C_{16–29}$ *n*-alkanes; Pr = pristane; Ph = phytane; *i*-C_{21} = C_{21} regular isoprenoid; C_{31}-H = C_{31} hopanes; β-c = β-carotane.

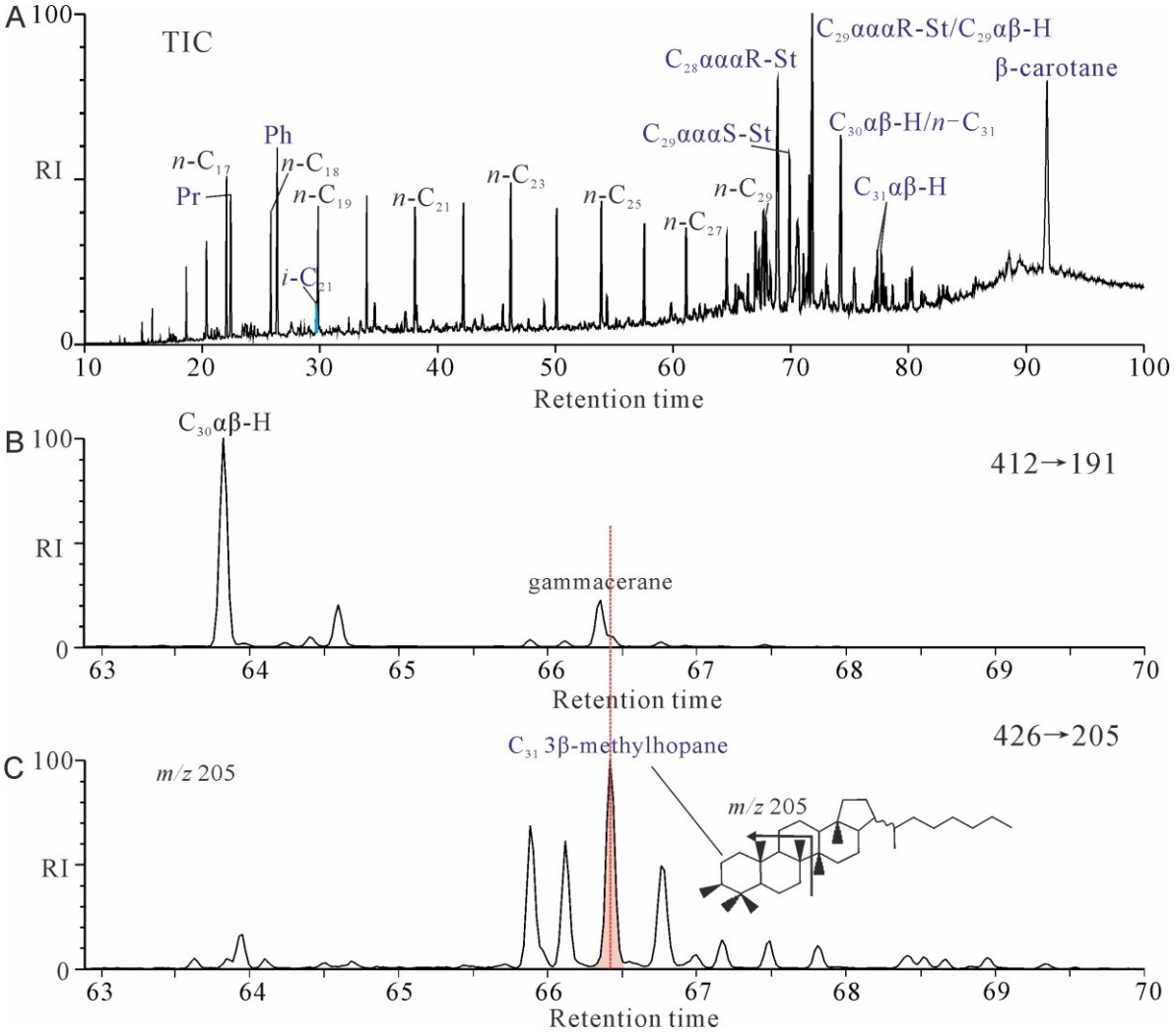

Fig. S2. Typical total ion chromatograms and some MRM-GC-MS chromatograms of organic matter in the Fengcheng Formation (well F20; 3152.3 m depth) (Xia et al., 2021b). (A) Total ion current (TIC) of the saturated hydrocarbon fraction; (B) *m/z* = 412–191 (MRM-GC-MS); (C) *m/z* = 426–205 (MRM-GC-MS) showing C_{31} 3β-methylhopane peaks near gammacerane.

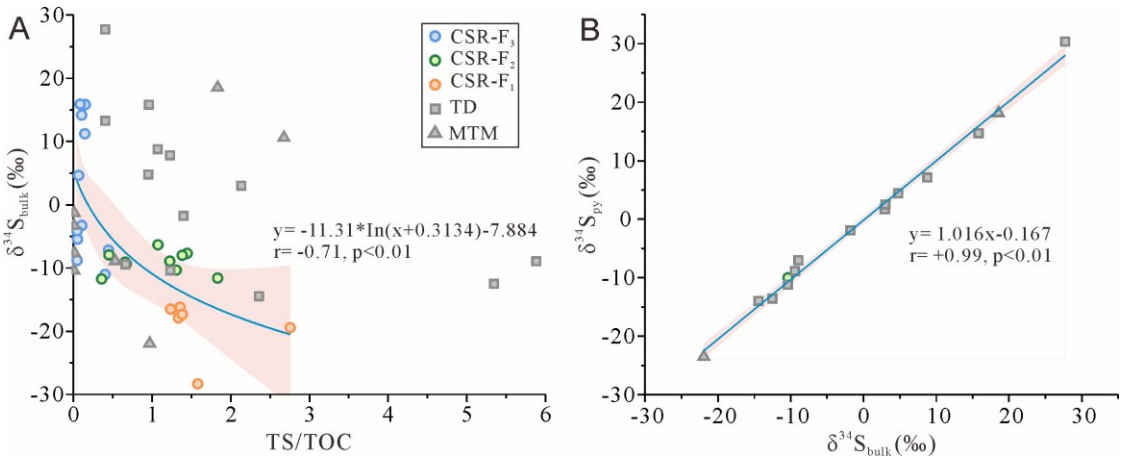

Fig. S3. Plots of (A) whole-rock S isotope data ($\delta^{34}S_{bulk}$) versus TS/TOC ratios and (B) whole-rock S isotope data ($\delta^{34}S_{bulk}$) versus pyrite S isotope data ($\delta^{34}S_{py}$). The trend lines were calculated with Origin 2023 software and show 95% confidence intervals (pink shaded areas), with all the p-values are <0.01.

Table S1. Geochemical data for the Fengcheng Formation in the Mahu Sag, Junggar Basin, including 3β-MeHI, $\delta^{13}C_{org}$, $\delta^{13}C_{carb}$, TS/TOC, and $\delta^{34}S_{bulk}$ values. A = average, N = number of samples, and SD = standard deviation. 3β-MeHI data are from (Xia et al., 2021b), and $\delta^{13}C_{org}$, $\delta^{13}C_{carb}$, and TS/TOC data are from (Xia et al., 2020). F_1, F_2, F_3 are the first, second, and third members of the Fengcheng Formation, respectively.

Area / Proxies	CSR (Wells F20, FN3, FN5, FN7, AK1)			TD (Wells F5, FN1, FN14)	MTM (Wells X40, X76, X87)
3β-MeHI (%)	2.9–14.2, A= 7.0, N= 15, SD= 3.3			3.1–8.8, A = 5.4, N = 3, SD = 3.0	2.3–6.0, A= 4.1, N= 2, SD= 2.7
	F_1	F_2	F_3		
	3.8–10.8, A= 7.7, N= 3, SD = 3.6	2.9–9.5, A= 4.9, N= 7, SD = 2.3	5.8–14.2, A= 9.5, N= 5, SD= 3.0		
$\delta^{13}C_{org}$ (‰)	-30.6–-25.7, A=-27.7, N= 28, SD= 1.2			-30.5–-26.1, A= -27.7, N = 14, SD = 1.2	-30.1–-24.8, A= -27.7, N = 8, SD = 1.7
	F_1	F_2	F_3		
	-27.2–-25.9, A= -26.7, N= 6, SD= 0.5	-28.8–-26.7, A= -27.9, N= 10, SD= 0.6	-30.6–-25.7, A= -28.0, N= 12, SD= 1.5		
$\delta^{13}C_{carb}$ (‰)	1.4–5.8, A= 3.3, N= 28, SD= 1.3			2.0–6, A= 4.2, N= 14, SD = 1.4	-3.8–0.5, A= -1.4, N= 8, SD= 1.9
	F_1	F_2	F_3		
	1.5–2.9, A= 2.3, N= 6, SD= 0.5	1.4–3.3, A= 2.3, N= 10, SD= 0.6	3.5–5.8, A= 4.5, N= 12, SD= 0.8		
	0.05–2.8, A= 0.8, N= 28, SD= 0.7				

TS/TOC	F_1	F_2	F_3	0.4–5.9, A= 1.9, N= 14, SD = 1.8	0.01–2.7, A= 0.8, N= 8, SD= 1.0
	1.2–2.8, A= 1.6, N= 6, SD= 0.6	0.4–1.8, A=1.0, N= 10, SD= 0.5	0.05–0.5, A= 0.2, N= 12, SD= 0.1		
$\delta^{34}S_{bulk}$ (‰)	-28.3–15.9, A = -6.2, N = 28, SD = 11.3			-14.4–27.7, A = 1.9, N= 14, SD = 12.3	-22.0–18.5, A= -3.0, N= 8, SD= 12.7
	F_1	F_2	F_3		
	-28.3–-16.2, A= -19.3, N= 6, SD= 4.6	-11.7–-6.3, A= -9.1, N= 10, SD= 1.7	-11.0–15.9, A= 2.8, N= 12, SD= 10.5		

Table S2. List of samples investigated in this study. F_1 = First Member of the Fengcheng Formation; F_2 = Second Member of the Fengcheng Formation; F_3 = Third Member of the Fengcheng Formation.

No.	**Well**	**Member**	**Depth/m**	**No.**	**Well**	**Member**	**Depth/m**
1	F20	F_3	3138.3	27	AK1	F_1	5663
2	F20	F_3	3139.1	28	AK1	F_1	5664.3
3	F20	F_3	3151.3	29	AK1	F_1	5665.9
4	F20	F_3	3152.3	30	AK1	F_1	5668
5	F20	F_3	3162	31	F5	F_3	3194.4
6	F20	F_3	3187.9	32	F5	F_2	3250
7	F20	F_3	3188.8	33	F5	F_2	3220.8
8	F20	F_3	3248	34	F5	F_2	3437
9	F20	F_3	3248.8	35	FN1	F_3	4096.5
10	F20	F_3	3250.5	36	FN1	F_2	4238.4
11	F20	F_3	3251.1	37	FN1	F_2	4341.8
12	F20	F_3	3268	38	FN1	F_1	4423.1
13	FN3	F_3	3958	39	FN1	F_1	4450.6
14	FN3	F_2	4127	40	FN14	F_3	4065.2
15	FN5	F_2	4066.3	41	FN14	F_3	4082.3
16	FN5	F_2	4065.5	42	FN14	F_3	4095
17	FN5	F_2	4068.9	43	FN14	F_3	4112.6
18	FN5	F_2	4069	44	FN14	F_2	4166.8
19	FN5	F_2	4071	45	X40	F_3	4577.7
20	FN7	F_2	4590.8	46	X40	F_3	4578.5
21	FN7	F_2	4595	47	X40	F_3	4581.5
22	FN7	F_2	4592	48	X40	F_2	4638.4

23	FN7	F_2	4596.2	49	X40	F_2	4764.5
24	FN7	F_2	4598.5	50	X76	F_1	3645.6
25	AK1	F_1	5661.5	51	X76	F_3	3455.5
26	AK1	F_1	5662	52	X87	F_1	4154